Reduced graphene oxide-supported aggregates of CuInS$_2$ quantum dots as an effective hybrid electron acceptor for polymer-based solar cells

Weili Meng [a, b], Xun Zhou [a], Zeliang Qiu [a], Changwen Liu [a], Junwei Chen [a, b], Wenjin Yue [c], Mingtai Wang [a, *], Hong Bi [d, **]

[a] Institute of Applied Technology, Hefei Institutes of Physical Science, Chinese Academy of Sciences, Hefei 230031, PR China
[b] University of Science and Technology of China, Hefei 230026, PR China
[c] School of Biochemical Engineering, Anhui Polytechnic University, Wuhu 241000, PR China
[d] College of Chemistry and Chemical Engineering, Anhui University, Hefei 230039, PR China

A B S T R A C T

A hybrid featuring the CuInS$_2$ quantum dots (CuInS$_2$-QDs) on reduced graphene oxide (rGO) sheets is synthesized by a facile one-pot solvothermal approach with thiourea as S source, in which graphene oxide (GO) sheets are reduced into rGO sheets in course of the CuInS$_2$-QDs aggregate growth. The growth mechanism of the hybrid is elucidated. It is found that adsorption of Cu^{2+} cations mainly takes place at epoxy/hydroxyl groups on GO sheets at room temperature and the adsorbed Cu$^+$ cations resulting from the Cu^{2+} reduction at solvothermal temperature act as the nucleation for the surface growth of CuInS$_2$-QDs into three-dimensional aggregates on GO sheets that are simultaneously reduced into rGO sheets. Our results demonstrate that the rGO/CuInS$_2$-QDs hybrid is an effective electron acceptor with a complementary absorption property for polymer-based solar cells. The solar cells based on rGO/CuInS$_2$-QDs hybrid and poly(1-methoxy-4-(2-ethylhexyloxy)-p-phenylene vinylene) exhibit an efficiency of 1.5%, much higher than the counterpart devices of rGO sheets. The effects of CuInS$_2$-QDs aggregates on device performance are discussed. In the long run, this work provides a potential hybrid electron acceptor for low-cost and efficient solar cell fabrication.

© 2015 Elsevier Ltd. All rights reserved.

1. Introduction

Polymer-based solar cells (PSCs) with a conjugated polymer as electron donor (D) and nanostructured semiconductor as electron acceptor (A) are attractive for low-cost, large area and even flexible solar cells [1–2]. In principle, PSCs work by the following steps: the polymer mainly absorbs photons to generate excitons (bound electron–hole pairs), the photogenerated excitons diffuse to the D/A interface for dissociation into free charge carriers (electrons and holes), and the free charge carriers are transported within D and A components to the respective electrodes for photocurrent generation. Accordingly, the broad spectral response range of materials, the formation of stably distributed D/A interfaces with a large interfacial area for effective exciton dissociation, and the formation of efficient charge transport channels are crucially important for achieving a high efficiency.

Graphene has been of great interests in fundamental research and practical application for its large specific surface area (2630 m^2 g^{-1}) [3], high mobility of charge carriers (2,00,000 cm^2 v^{-1} s^{-1}) [4], superior mechanical strength with a high Young's modulus (~1.0 TPa) [5], superior thermal conductivity (~5000 W m^{-1} K^{-1}) [6], good optical transmittance (~97.7%) [7], and good flexibility and chemical stability. These excellent properties support the wide graphene applications to such as electronics, energy fields, sensors and catalysts [8]. Graphene has been applied to the PSCs that use fullerene derivatives (e.g., PC$_{61}$BM and PC$_{71}$BM) as electron acceptor, where the graphene serves as the transparent electrode [9,10], hole transporter layer [11], and hole/electron extraction layer [12-14]. Alternatively, organics-modified and soluble graphene has been used as the electron acceptor and produces the graphene-based PSCs with a power conversion

efficiency (η) up to 1.4% [15,16]. Replacing the fullerene molecules with graphene can provide large donor/acceptor interfaces for charge generation and a continuous pathway for electron transport. However, the graphene-based PSCs still suffer from some deficiencies, such as (i) the rather narrow absorption spectrum and short exciton diffusion length in common polymers; (ii) the serious agglomeration of graphene sheets does not favor the formation of polymer/graphene interface that is necessarily important for exciton dissociation, and (iii) the preferred flat-on configuration with graphene sheets lying parallel to the film plane is unfavorable to the charge transfer for photocurrent generation.

Graphene is a good matrix to support functional nanoparticles. The hybrids with the nanoparticles or quantum dots (QDs) of metals (e.g., Au, Ag and Pt), metal oxides (e.g., ZnO, TiO_2, Fe_3O_4, SnO_2, Cu_2O, MnO_2 and NiO) and chalcogenides (e.g., CdS, ZnS, Cu_2S, MoS_2, Sn_3S_4 and CdTe) on graphene sheets have been synthesized as the potential materials for optoelectronic, magnetic, catalytic and biomedical applications [17–23]. Graphene/nanoparticle hybrids can be synthesized by the in situ growth of nanocrystals on graphene sheets or the adsorption of preformed nanocrystals onto graphene sheets. The adsorption approach often results in the graphene sheets decorated by nanoparticles with a limited loading density [17,23]; however, the in situ growth strategy can produce the high surface coverage of nanocrystals on graphene sheets with a three-dimensional (3-D) architecture [18,21].

Copper indium disulfide ($CuInS_2$) is a promising light-absorbing material for solar cells due to its small direct band gap of 1.5 eV that matches well solar spectrum, high absorption coefficient of 10^5 cm^{-1} and low toxicity [24,25]. We have previously reported the solvothermal synthesis of chalcopyrite $CuInS_2$ nanoparticles [26] and QDs [27], as well as zinc blende $CuInS_2$-QDs [28]. Our results demonstrated that those $CuInS_2$-QDs can serve as the effective electron acceptor for PSCs [27,28]. The PSCs based on the polymer/$CuInS_2$ materials are mainly prepared by blending $CuInS_2$-QDs with a conjugated polymer in solutions [28–30] or by in situ synthesis of $CuInS_2$-QDs in polymer solutions [31–33]; in particular, the polymer/$CuInS_2$-QDs devices have reached the efficiencies up to 1.6–2.8% when using a high weight fraction of $CuInS_2$-QDs and a small band gap polymer (e.g., conjugated polymers derived from benzothiadiazole) in the photoactive layer [31,33].

The hybrids consisting of chalcopyrite $CuInS_2$ nanocrystals (ca. 100 nm in diameter) on reduced graphene oxide (rGO) sheets have been synthesized via a two-step hydrothermal route for dye-sensitized solar cells [34]. The microscale flower-like $CuInS_2$ particles on rGO sheets were prepared by a one-pot solvothermal method and used as a photoelectrochemcial biosensor for H_2O_2 detection [35]. However, there has been no report on the in situ growth of 3-D $CuInS_2$-QDs aggregates on graphene sheets. In this paper, we synthesized a rGO/$CuInS_2$-QDs hybrid by a facile one-pot solvothermal method and the growth mechanism of the hybrid is revealed; moreover, it is demonstrated that the rGO/$CuInS_2$-QDs hybrid is an effective hybrid electron acceptor with a complementary absorption property for PSCs.

2. Experimental section

2.1. Chemicals

Indium acetate ($In(Ac)_3$) (99.99%, Aldrich), 1-octadecylamine (98%, Alfa Aesar), poly(1-methoxy-4-(2-ethylhexyloxy)-p-phenylenevinylene) (MEH-PPV) (average Mn = 40,000–70,000, Aldrich), poly (3, 4-ethylenedioxythiophene):poly (styrene sulfonate) (PEDOT:PSS) (Clevios™ PH 1000) and graphite powder (Aladdin) were commercially obtained. Other chemicals, including cupric acetate monohydrate ($Cu(Ac)_2 \cdot H_2O$) (AR), cupric chloride ($CuCl_2$) (AR), thiourea (AR), ethanol (AR), acetone (AR), isopropylalcohol (AR), hydrochloric acid (AR), chlorobenzene (CP), were purchased from the Sinopharm Chemical Reagent Co., Ltd. All the chemicals were used without further purification, except for the distillation of chlorobenzene under reduced pressure before use.

2.2. Synthesis of rGO/$CuInS_2$-QDs hybrid

Graphene oxide (GO) was prepared by a Hummers method [36], and was dried at 60 °C under vacuum for 24 h before use. The rGO/$CuInS_2$-QDs hybrid was prepared as follows. A certain amount (5 mg) of GO was dispersed in 80 mL absolute ethanol by ultrasonication to obtain a homogeneous suspension. Then, $Cu(Ac)_2 \cdot H_2O$ (0.1 mmol), $In(Ac)_3$ (0.1 mmol), and 1-octadecylamine (1.2 mmol), were dissolved/dispersed into a blue suspension by ultrasonic treatment. Finally, $CS(NH_2)_2$ (0.4 mmol) was added into the dispersion and a brown-black dispersion was rapidly produced, which was used as the precursor for the synthesis of the rGO/$CuInS_2$-QDs hybrid. The precursor dispersion was transferred into a 100 mL Teflon-lined autoclave and heated at 160 °C for 12 h. The solid precipitate was obtained by centrifuge (9000 rpm, 10 min), washed with absolute ethanol at least three times and dried in vacuum at 60 °C for 6 h prior to other measurements. For comparison, pristine rGO was prepared through a similar solvothermal procedure in ethanol when without all of the chemicals for $CuInS_2$ growth, while the $CuInS_2$-QDs were prepared by the similar solvothermal procedure in the absence of GO.

2.3. Solar cell fabrication

Indium tin oxide-coated glass (ITO, ≤ 15 $\Omega/\square$, Shenzhen Laibao Hi-Tech Co., Ltd, China) was first patterned into stripes (16×4 mm^2) on the glass substrate by HCl solution and Zn powder, and washed twice with acetone, isopropanol, and deionized water, respectively. A condensed TiO_2 film (ca. 40 nm in thickness) as hole blocking layer (HBL) was prepared on ITO by the procedure described previously [37]. The MEH-PPV/rGO-$CuInS_2$ solar cells were prepared as follows. The MEH-PPV/rGO-$CuInS_2$ blend layer was coated on the TiO_2 film by spin-coating (1000 rpm, 60 s) the MEH-PPV solution in chlorobenzene (10 mg/mL) which had been added the rGO/$CuInS_2$-QDs hybrid (17% by weight), and annealed at 160 °C for 10 min under N_2 atmosphere. Afterward, a PEDOT:PSS film (ca. 80 nm in thickness) was spin-coated (1000 rpm, 60 s) over the MEH-PPV/rGO-$CuInS_2$ active layer, for which the PEDOT:PSS solution with isopropanol (50% in volume) was filtered with a 0.80 μm filter after an ultrasonic treatment for 15 min prior to use. After the deposition of PEDOT:PSS film, the sample was thermally annealed at 100 °C for 30 min under N_2 atmosphere. Finally, Au electrode with the thickness of 100 nm was thermally evaporated over PEDOT:PSS film through a shadow mask to form a top contact of 1×4 mm^2, which defined the active area of each device. The devices were sealed in a glovebox ($O_2 \leq 1$ ppm, $H_2O \leq 1$ ppm) under a N_2 atmosphere. For comparison, the MEH-PPV/rGO solar cells were also prepared by using pristine rGO (17% by weight) instead of rGO/$CuInS_2$-QDs hybrid.

2.4. Instruments and characterizations

X-ray diffraction (XRD) patterns were recorded on a Philips X'Pert Pro X-ray diffractometer with Cu Kα radiation ($\lambda = 1.541841$ Å). Transmission electron microscopy (TEM) and high-resolution TEM (HRTEM) studies were carried out on a JEOL-2010 microscopy under an acceleration voltage of 200 kV. X-ray photoelectron spectroscopy (XPS) analyses were performed on an ESCALAB 250 XPS, using an Al Kα X-ray as the excitation source, and

all the XPS peaks were calibrated by using the C1s peak (284.60 eV) for neutral carbon as the reference. Raman spectroscopy was performed using a Raman Microprobe (Labram-HR Jobin-Yvon, France) with a laser wavelength of 514.5 nm. Fourier transform infrared (FT−IR) spectra of the samples in KBr pellets were recorded on a Nicolet Magna-IR™ 750 spectrometer with a maximum resolution of 0.1 cm^{-1}. Cyclic voltammetric (CV) measurements were performed on an IM6e electrochemical workstation (Zahner Co., Germany) at a scan rate of 50 mV/s, with a platinum wire as counter electrode. In the CV measurements, tetrabutylammonium perchlorate dissolved in acetonitrile (0.1 M) was used as supporting electrolyte, and the potential (E) was recorded versus Ag/AgCl reference electrode. The working electrode was prepared by drying a drop of CuInS$_2$-QDs dispersion (0.04 mg/mL) in ethanol on a glassy carbon discs that had been freshly polished, cleaned and dried. The electrolyte solution was first thoroughly deoxygenated by bubbling high purity nitrogen for 15 min, and a nitrogen atmosphere was maintained during the CV measurements.

The pristine MEH-PPV film and the MEH-PPV/rGO and MEH-PPV/rGO-CuInS$_2$ blend films for optical measurement were prepared on freshly cleaned quartz substrates by spin-coating (1000 rpm, 60 s) the MEH-PPV solution in chlorobenzene (5 mg/mL), which was added rGO or rGO-CuInS$_2$ for preparing blend films. Absorption spectra were recorded under ambient conditions on a UV 2550 spectrophotometer (Shimadzu) and photoluminescence (PL) spectra were measured under ambient conditions on a F−7000 spectrofluorometer (Hitachi) with excitation at 480 nm. Current−voltage (J−V) characteristics of solar cells were measured under AM1.5 illumination with an intensity of 100 mW/cm^2 from a 94023A Oriel Sol3A solar simulator (Newport Stratford, Inc.), and the light intensity from a 450 W xenon lamp was calibrated with a standard crystalline silicon solar cell; the J−V curves were collected with an Oriel® I−V test station (PVIV-1A, Keithley 2400 Source Meter, Labview 2009 SP1 GUI Software, Newport). Incident photon-to-current efficiency (IPCE) spectra of solar cells were recorded on a QE/IPCE Measurement Kit (Newport, USA) that was automatically controlled by Oriel® Tracq Basic V5.0 software with the light from a 300 W xenon lamp focused through a monochromator (74125 Oriel Cornerstone 260 1/4 m) onto the solar cells under test, where light intensity and photocurrent generated were measured with a 2931-C dual channel power/current meter and 71675 calibrated UV silicon photodetector.

3. Results and discussion

3.1. Characterization of rGO/CuInS$_2$-QDs hybrid

Shown in Fig. 1 are the XRD patterns of samples. Our GO sample exhibits the characteristic peaks at $2\theta = 10.6°$ and $43.0°$, corresponding to the (001) and (111) plane reflections, respectively [38,39]. The interplanar spacing in the GO sheets is calculated from the Bragg equation to be 0.79 nm. As for the rGO sample, it shows the typical reflection peaks of rGO at $2\theta = 23.7°$, and $43.0°$ from (002) and (111) planes, respectively [40,41]. The interplanar spacing of 0.37 nm is obtained for the rGO sample. Clearly, GO can be reduced into rGO in the solvothermal process without CuInS$_2$ precursor. Further evidences for the reduction of GO in the solvothermal process are provided by FT−IR and Raman spectra (Figs. S1 and S2). The vibration peaks related to the epoxy/hydroxyl groups (i.e., C−OH and C−O−C) in the FT−IR spectrum of rGO sheets were greatly reduced with respect to those of GO (Fig. S1); moreover, rGO displayed a higher intensity ratio between D band and G band (I_D/I_G), indicating the formation of smaller in-plane sp^2 domains during the GO reduction (Fig. S2). Therefore, the majority of epoxy/hydroxyl groups are removed from GO sheets during the
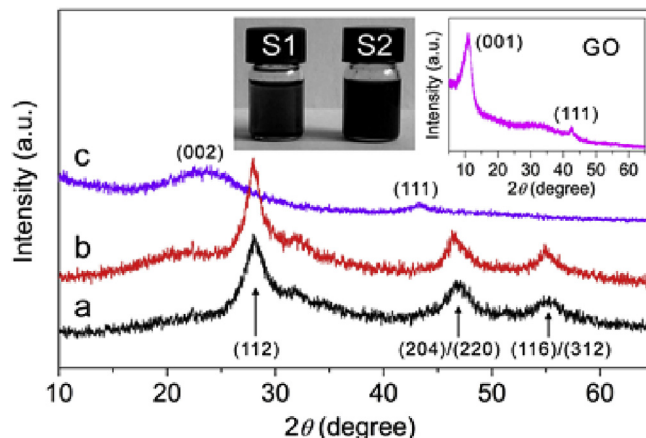

Fig. 1. XRD patterns of (a) CuInS$_2$-QDs, (b) rGO/CuInS$_2$-QDs hybrid and (c) rGO. The insets show the XRD pattern of GO and the photograph of rGO/CuInS$_2$-QDs hybrid dispersions in chloroform (S1) and chlorobenzene (S2) taken 6 h later after dispersion formation. (A color version of this figure can be viewed online.)

solvothermal reduction process, which also leads to the decrease in interplanar spacing [41].

The pristine CuInS$_2$-QDs obtained in the solvothermal process display the diffraction peaks at $2\theta = 27.9°$, 46.5° and 55.0° that match well the (112), (204) or (220), and (116) or (312) crystal planes of chalcopyrite CuInS$_2$ (JCPDS Card #85−1575, a = b = 5.523 Å and c = 11.133 Å), in agreement with our previous report [27]. The XRD pattern of rGO/CuInS$_2$-QDs hybrid is similar to that of the pristine CuInS$_2$-QDs. The typical peak of rGO around 23.7° is absent in rGO/CuInS$_2$-QDs hybrid. The disappearance of the (002) diffraction peak of rGO in the hybrid indicates the destruction of the regular stacks of graphene sheets by exfoliation or intercalation of reactants [42,43]. The average size (S) of CuInS$_2$ nanocrystals was estimated by Scherrer formula. The as-synthesized CuInS$_2$ nanocrystals in the pristine CuInS$_2$-QDs and rGO/CuInS$_2$-QDs hybrid are actually quantum dots with an average diameter of 3.3 and 4.6 nm, respectively. The rGO/CuInS$_2$-QDs hybrid displays a stable colloidal dispersion in organic solvents (inset to Fig. 1), which will facilitate their practical applications under an organic-solution condition. Our XPS data showed that the stoichiometric ratio of Cu:In:S was 1.31:1.00:1.86 in the rGO/CuInS$_2$-QDs hybrid (Fig. S3).

HRTEM image (Fig. 2a) shows that the pristine CuInS$_2$-QDs prepared by the solvothermal process without GO in situ are almost spherical with a size of 2−5 nm, and the lattice fringes match the spacing distance of (112) crystal planes of chalcopyrite CuInS$_2$ ($d_{(112)} = 0.31969$ nm). The TEM image of rGO/CuInS$_2$-QDs hybrid (Fig. 2b) clearly shows the CuInS$_2$-QDs aggregates on the rGO sheet. Two typical regions (regions 1 and 2 as marked) were observed by HRTEM, revealing two kinds of aggregation morphology of CuInS$_2$-QDs. In region 1 where no obvious nanoparticle aggregates are present (Fig. 2c), the rGO sheets are actually decorated by the separated CuInS$_2$-QDs of 2−5 nm in diameter. However, the CuInS$_2$-QDs in region 2 (Fig. 2d) aggregate into irregular 3-D networks with continuous and highly condensed nanochannels of 2−10 nm in width with a widely distributed length. CuInS$_2$-QDs in both region 1 and 2 exhibit the lattice fringes of the (112) crystal planes of chalcopyrite CuInS$_2$. Noticeably, no CuInS$_2$-QDs was found on the TEM grid outside rGO sheet, even though similarly sized CuInS$_2$-QDs grown in solution when without GO were able to be collected by the centrifugation procedure same to that for collecting the hybrid, indicating that a strong interaction between CuInS$_2$-QDs (or CuInS$_2$-QDs aggregates) and rGO matrix and a surface growth of
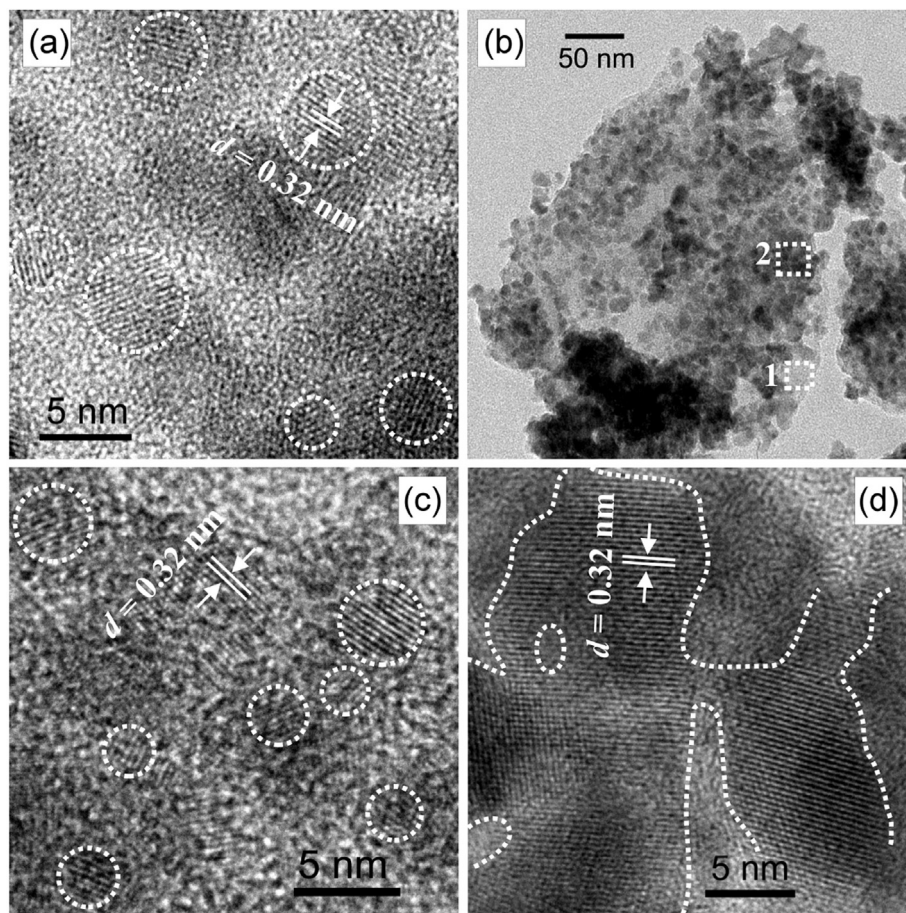
Fig. 2. (a) CuInS$_2$-QDs and (b–d) rGO/CuInS$_2$-QDs hybrid imaged by TEM (b) and HRTEM (a, c, d). Two typical regions are identified on the TEM image of rGO/CuInS$_2$-QDs hybrid, that is, region 1 illustrates the locations where no nanoparticle aggregates are obviously present, while region 2 show the places with CuInS$_2$-QDs aggregating into 3-D networks. Images (c) and (d) are for the regions 1 and 2 on image (b), respectively. The circles on images (a) and (c) are used as a visual aid to show the individual quantum dots. The dotted lines on (d) identify the MEH-PPV/CuInS$_2$ interfaces and CuInS$_2$-QDs channels.

CuInS$_2$-QDs aggregates on graphene sheets.

Fig. 3 compares the absorption spectra of rGO, CuInS$_2$-QDs and rGO/CuInS$_2$-QDs hybrid. rGO sheets only exhibit a very weak absorption in the 300–900 nm region, similar to the previous reports [44]. The absorption spectrum of the pristine CuInS$_2$-QDs (2–5 nm in size) prepared when without GO sheets in situ is characterized by a broad shoulder with a trail in the long-wavelength direction
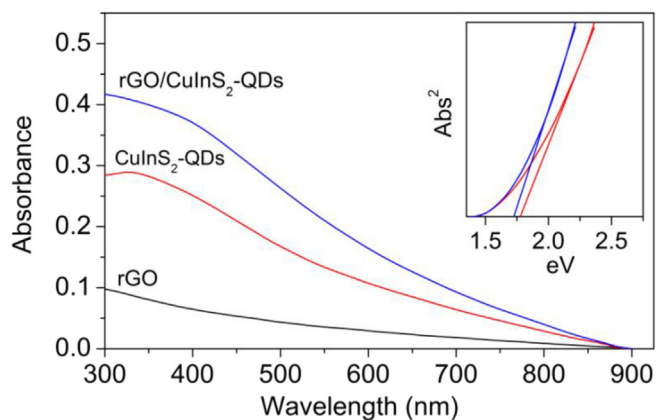

Fig. 3. Absorption spectra of rGO, CuInS$_2$-QDs and rGO/CuInS$_2$-QDs hybrid dispersed in ethanol (0.05 mg/mL). (A color version of this figure can be viewed online.)

typically up to 900 nm, which is consistent with our previous reports [27]. The band gap of the pristine CuInS$_2$-QDs is approximated to be 1.77 eV, using a direct band gap method [45,46] by plotting the squared absorbance versus energy and extrapolating to zero (inset to Fig. 3). The optical band gap agrees well with the electrochemical band gap (1.76 eV) of the CuInS$_2$-QDs measured by CV method (Fig. S4). Clearly, the band gap of CuInS$_2$-QDs is significantly blue-shifted as compared to that of bulk CuInS$_2$ (1.53 eV) due to the quantum size effect [47]. The rGO/CuInS$_2$-QDs hybrid exhibits mainly the typical absorption features of the CuInS$_2$-QDs, with a band gap of ca. 1.73 eV. Obviously, the absorption of rGO/CuInS$_2$-QDs hybrid is still dominated by the CuInS$_2$-QDs with a size of ca. 2–5 nm.

3.2. Formation mechanism of rGO/CuInS$_2$-QDs hybrid

In order to get insight into the formation processes for rGO/CuInS$_2$-QDs hybrid, we carried out the XPS studies of samples. Fig. 4 shows the C1s XPS spectra of GO, rGO, and rGO/CuInS$_2$-QDs samples. GO sheet surfaces normally contain carboxyl (COOH), epoxy (C–O–C) and hydroxyl (C–OH) groups [48]. The C1s XPS spectrum of GO sheets (Fig. 4a) shows the peaks at 284.6, 286.8, and 288.6 eV, which correspond to neutral (C–C), ether (C–O), and carboxyl (O=C–O) carbons, respectively [49,50]. To quantitatively study the change in the concentration of functional groups, we here use the integrated area to express the peak intensity, and the relative
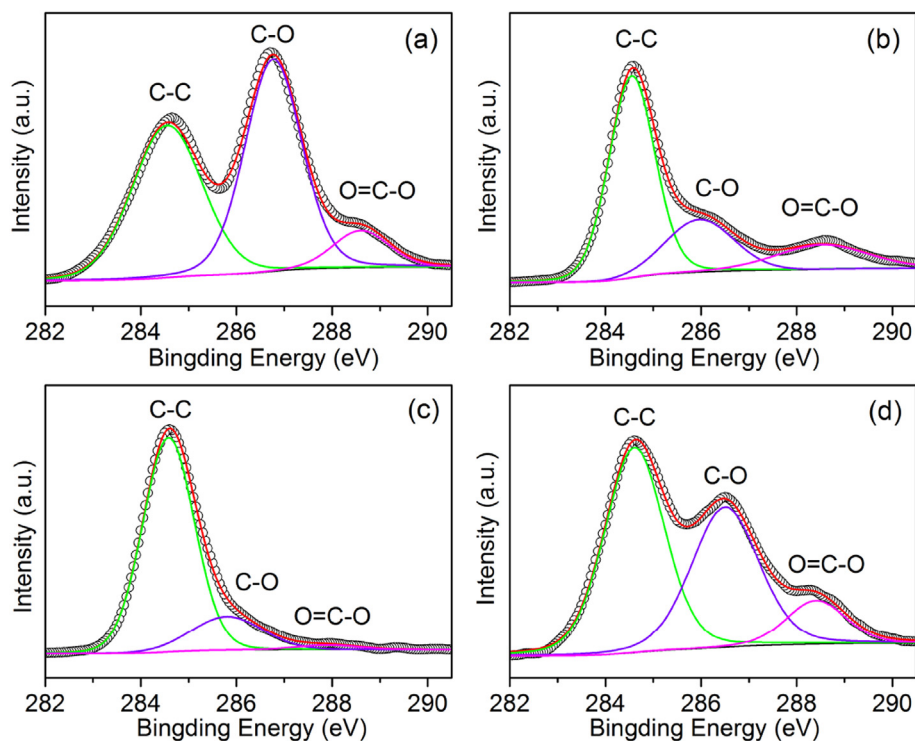
Fig. 4. The C1s XPS spectra of (a) GO, (b) rGO, (c) rGO/CuInS$_2$-QDs hybrid and (d) GO/Cu(Ac)$_2$. Sample GO/Cu(Ac)$_2$ was prepared as follows: GO sheets were first soaked in the ethanol solution (0.06 mg/mL) of cupric acetate monohydrate for 2 h under stirring; afterward, the GO sheets with adsorbed Cu^{2+} cations were isolated from the solution by centrifugation (9000 rpm, 5 min), washed with ethanol and dried at 60 °C in vacuum overnight. (A color version of this figure can be viewed online.)

fractions of ether (f_{C-O}) and carbonyl ($f_{O=C-O}$) carbons in the samples are evaluated from their intensities with respect to that of neutral carbons [51], that is, $f_{C-O} = A_{C-O}/A_{C-C}$ and $f_{O=C-O} = A_{O=C-O}/A_{C-C}$ (Table 1). We get $f_{C-O} = 1.16$ and $f_{O=C-O} = 0.19$ for the ether and carboxyl carbons on the GO sheets, respectively. The rGO (Fig. 4b) also exhibits the peaks for neutral, ether and carboxyl carbons. Comparison between the C1s XPS data of GO and rGO sheets shows that the relative fractions of ether carbons on the rGO sheets are greatly reduced to $f_{C-O} = 0.38$, but the $f_{O=C-O}$ value of carboxyl carbons is almost unchanged similar to the observations by others [44]. Clearly, it is mainly the epoxy/hydroxyl (i.e., C–OH and C–O–C) groups that are reduced in the solvothermal process in the absence of CuInS$_2$ precursor. In the rGO/CuInS$_2$-QDs hybrid (Fig. 4c), the fractions of f_{C-O} (0.21) and $f_{O=C-O}$ (0.03) are much smaller than those in the rGO, indicating that growth of CuInS$_2$-QDs aggregates facilitates the reduction of both ether and carboxyl groups on GO sheets in the solvothermal process.

In the precursor for the synthesis of rGO/CuInS$_2$-QDs hybrid, some Cu^{2+} cations will be adsorbed onto GO sheets, leading to the presence of adsorbed and free Cu^{2+} cations in the precursor

Table 1
Relative fractions of ether and carboxyl carbons on graphene sheets in different samples.[a]

Sample	GO	rGO	rGO/CuInS$_2$-QDs[b]	GO/Cu(Ac)$_2$[b]	GO/CuCl$_2$[b]
f_{C-O}	1.16	0.38	0.21	0.77	0.77
$f_{O=C-O}$	0.19	0.23	0.03	0.21	0.17

[a] In the XPS data analysis, C1s peak deconvolution was performed by using a Gaussian–Lorentzian peak shape after a Shirley background subtraction.
[b] Samples rGO/CuInS$_2$-QDs and GO/Cu(Ac)$_2$ are the same to those in Fig. 4; the method for preparing sample GO/CuCl$_2$ was the same to that for GO/Cu(Ac)$_2$, except for the replacement of Cu(Ac)$_2$·H$_2$O with CuCl$_2$.

dispersion (Fig. S5). The carboxyl and epoxy/hydroxyl groups on GO sheets can serve as the functional sites for chemical reaction [48]. To study the growth of CuInS$_2$-QDs aggregates on GO sheets and its effects on the GO reduction during solvothermal process, we measured the XPS spectrum of the GO sheets after soaking in ethanol solution of cupric acetate monohydrate (sampled as GO/Cu(Ac)$_2$). The C1s spectrum of GO/Cu(Ac)$_2$ (Fig. 4d) shows a decreased f_{C-O} in comparison to that for GO (Table 1), and the decrease in f_{C-O} suggests the absorption of Cu^{2+} cations at the epoxy/hydroxyl groups [49,52]. However, sample GO/Cu(Ac)$_2$ shows a little bit higher $f_{O=C-O}$ than GO (Table 1). We replaced cupric acetate monohydrate with CuCl$_2$ to carry out the adsorption of Cu^{2+} on GO sheets (sampled as GO/CuCl$_2$), the C1s XPS spectrum of the GO/CuCl$_2$ (Fig. S6) exhibited the $f_{O=C-O}$ value of 0.17 that is very close to that in GO sample (Table 1). The XPS data for the adsorption of Cu^{2+} cations on GO sheets suggest that almost no adsorption of Cu^{2+} cations at carboxyl groups on GO sheets, and a bit higher $f_{O=C-O}$ in GO/Cu(Ac)$_2$ than in GO is evidently attributed to the presence of COOH groups from cupric acetate monohydrate. Reasonably, Cu^{2+} cations are merely adsorbed by epoxy/hydroxyl groups rather than carboxyl groups on GO sheets for growing rGO/CuInS$_2$-QDs hybrid.

Moreover, the Cu^{2+} cations in bulk solution can react easily with thiourea molecule into a Cu^{2+}-thiourea complex [Cu(II)-Tu] at room temperature [26]. Therefore, it should be clarified whether the adsorbed Cu^{2+} cations also react with thiourea to form complex. We also measured the Cu2p spectrum of GO sheets after soaking in ethanol solution containing both cupric acetate monohydrate and thiourea (sampled as GO/Cu(Ac)$_2$-Tu). The Cu2p spectra of samples GO/Cu(Ac)$_2$, GO/Cu(Ac)$_2$-Tu and rGO/CuInS$_2$-QDs are compared in Fig. 5. GO/Cu(Ac)$_2$ (trace a) shows the binding energies of Cu2p3/2 and Cu2p1/2 at 933.3 eV and 953.3 eV, respectively, with a Cu2p3/2 satellite peak centered at 942 eV, indicating the presence of Cu^{2+}
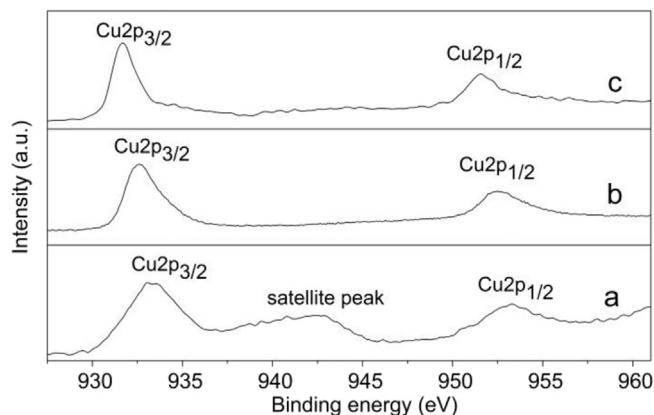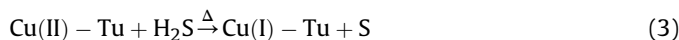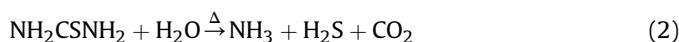
Fig. 5. Cu2p spectra of samples (a) GO/Cu(Ac)$_2$, (b) GO/Cu(Ac)$_2$-Tu and (c) rGO/CuInS$_2$-QDs hybrid.

cations [53]. Moreover, the core level spectrum of Cu2p in rGO/CuInS$_2$-QDs (trace c) is split into Cu2p3/2 at 931.7 eV and Cu2p1/2 at 951.6 eV, in agreement with the Cu$^+$ cations in the CuInS$_2$ previously reported [27]. However, GO/Cu(Ac)$_2$-Tu (trace b) has the Cu2p3/2 (932.6 eV) and Cu2p1/2 (952.5 eV) peaks different from either GO-Cu(Ac)$_2$ or rGO/CuInS$_2$-QDs, which indicates a different valence state of copper atoms in the GO/Cu(Ac)$_2$-Tu. We believe the adsorbed Cu^{2+} cations react with thiourea into Cu^{2+}-thiourea complexes, similar to the case of free Cu^{2+} cations in bulk solution.

The rGO/CuInS$_2$-QDs hybrid is evidently formed by following reactions,

$$Cu^{2+} + thiourea \rightarrow Cu(II) - Tu \tag{1}$$

$$NH_2CSNH_2 + H_2O \xrightarrow{\Delta} NH_3 + H_2S + CO_2 \tag{2}$$

$$Cu(II) - Tu + H_2S \xrightarrow{\Delta} Cu(I) - Tu + S \tag{3}$$

$$Cu(I) - Tu \xrightarrow{\Delta} Cu^+ \tag{4}$$

$$Cu^+ + In^{3+} + S^{2-} \xrightarrow{\Delta} CuInS_2 \tag{5}$$

First, the initial Cu^{2+} cations in solution are partially adsorbed onto GO sheets at epoxy/hydroxyl groups in preparing the precursor mixture, with some free Cu^{2+} leaving in solution. Then, the addition of thiourea (Tu) leads to a rapid color change from blue to brown-black without evident emission of H$_2$S (Experimental section), due to the formation of complex Cu(II)-Tu. During the solvothermal process, the resultant H$_2$S from the reaction between thiourea and trace water reduces the adsorbed and free Cu(II)-Tu into Cu$^+$-thiourea complexes [Cu(I)-Tu] [54—56], the resultant S is indicated by the production of slightly yellow solution in autoclave after solvothermal process; since In(Ac)$_3$ has a bad solubility in ethanol both at room temperature and even at the boiling point of ethanol (78 °C), In(Ac)$_3$ get dissolved in the solvothermal process to slowly release the In3+ cations cations into solution. Afterward, these Cu(I)-Tu are decomposed into Cu$^+$ cations [56]; the adsorbed Cu$^+$ cations nucleate the In^{3+} cations from the dissolved In(Ac)$_3$ and the resultant S^{2-} anions in solution to form the CuInS$_2$-QDs in situ on the surface of GO sheet, which serve as the nucleation for surface growth of CuInS$_2$-QDs into 3-D aggregates. Even though the solvothermal process may have reduced GO into rGO to a certain extent [44], the growth of CuInS$_2$-QDs aggregates helps the further

reduction of GO, eventually resulting in the rGO/CuInS$_2$-QDs hybrids (Fig. 2b). The presence of 1-octadecylamine as capping agent in the reaction mixture limits the growth of large CuInS$_2$ nanocrystals and facilitates the CuInS$_2$-QDs aggregate growth on graphene sheets. The formation mechanism of rGO/CuInS$_2$-QDs hybrid is depicted in Fig. 6.

3.3. Solar cells

Solar cells are fabricated using the MEH-PPV/rGO and MEH-PPV/rGO-CuInS$_2$ blends (in a weight ratio of 5:1) as photoactive layer (inset to Fig. 7a). The $J–V$ curves of the solar cells were measured under AM1.5 illumination (100 mW/cm^2) (Fig. 7a). Table 2 presents the overall photovoltaic performance of these devices. The MEH-PPV/rGO devices have a comparable short circuit current (J_{sc}) and open circuit voltage (V_{oc}) values but a higher fill factor (FF) in comparison to polymer/soluble-graphene devices with poly(3-hexyltiophene) (P3HT) as the polymer [16]. With respect to the MEH-PPV/rGO devices, the MEH-PPV/rGO-CuInS$_2$ cells exhibit a higher V_{oc}, J_{sc} and η. Moreover, the MEH-PPV/rGO-CuInS$_2$ devices have a higher V_{oc} but a lower J_{sc} than the solar cells based on P3HT:CuInS$_2$-QDs:rGO blends (with a weight ratio of 1:1:0.005; V_{oc} = 0.46 V, J_{sc} = 7.5 mA/cm^2) [57]; the reason for the lower J_{sc} in our cases may be due to a rather low CuInS$_2$-QDs content in photoactive layer.

Fig. 7b shows the energy level diagram for the MEH-PPV/rGO-CuInS$_2$ devices. The highest occupied molecular orbital (HOMO) (−5.3 eV) and lowest unoccupied molecular orbital (LUMO) (−3.0 eV) levels of MEH-PPV [58], the work-function (W_f) value for rGO (−4.2 eV) [59] are adopted by referring to the previous reports, and the valence (−5.8 eV) and conduction (−4.0 eV) band edges of CuInS$_2$-QDs were referred to data for similarly-sized pristine CuInS$_2$-QDs (Fig. S4). For efficient photocurrent generation, the neutral excitons generated by photoexcitation need to be separated into free charge carriers that further require the collection at device electrodes. According to the band alignments, the MEH-PPV/rGO and MEH-PPV/CuInS$_2$ interfaces are energetically favorable for the dissociation of the excitons generated by MEH-PPV absorption, while the CuInS$_2$/rGO interface provides the dissociation site for the excitons generated by CuInS$_2$-QDs absorption (Fig. 3). The MEH-PPV/rGO-CuInS$_2$ devices have reasonably three exciton dissociation processes as follows: (1) excitons generated in MEH-PPV dissociate at MEH-PPV/rGO interface, by directly injecting electrons into rGO with holes remaining in MEH-PPV; (2) excitons generated in MEH-PPV dissociate at the MEH-PPV/CuInS$_2$ interface, by injecting electrons into CuInS$_2$-QDs nanochannels with holes remaining in MEH-PPV, followed by the electron injection from CuInS$_2$-QDs nanochannels into rGO at CuInS$_2$/rGO interface; and (3) excitons generated in CuInS$_2$-QDs dissociate at the CuInS$_2$/rGO interface, by injecting electrons into rGO and holes into MEH-PPV. Finally, the electrons in rGO and the holes in MEH-PPV are collected by their respective electrodes for photocurrent generation.

Fig. 7c illustrates the nanomorphology in the photoactive layer of rGO/CuInS$_2$-QDs solar cells. As compared with the narrow absorption range (mainly in 400—600 nm) of MEH-PPV and MEH-PPV/rGO films, the MEH-PPV/rGO-CuInS$_2$ displays an extended absorption to ca. 900 nm due to the complementary absorption of CuInS$_2$-QDs (Fig. S7). In order to get insight into the photocurrent generation related to CuInS$_2$-QDs aggregate formation, the IPCE spectra of solar cells were measured (Fig. S8). The IPCE measurements indicate the absorption of CuInS$_2$-QDs contributes actually to photocurrent generation in the solar cells, even though weakly due to a quite small weight fraction of CuInS$_2$-QDs, resulting in the solar cells with a broad spectral response extending to 850 nm. Besides providing the complementary absorption for charge generation,
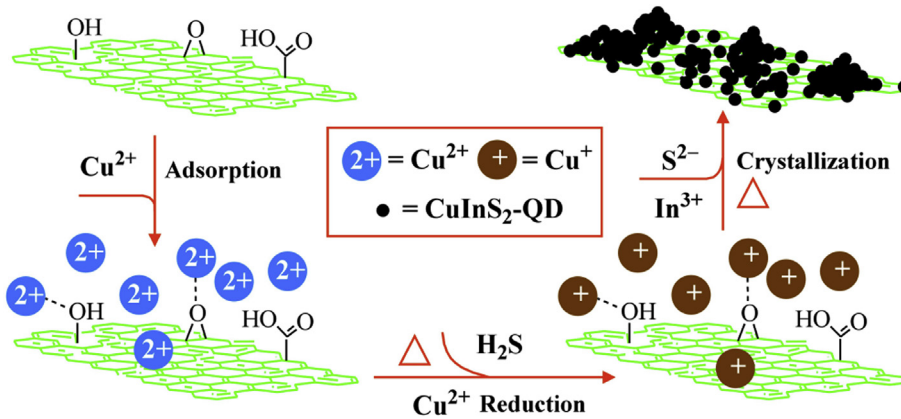
Fig. 6. Schematic illustration for the formation of rGO/CuInS$_2$-QDs hybrid. (A color version of this figure can be viewed online.)
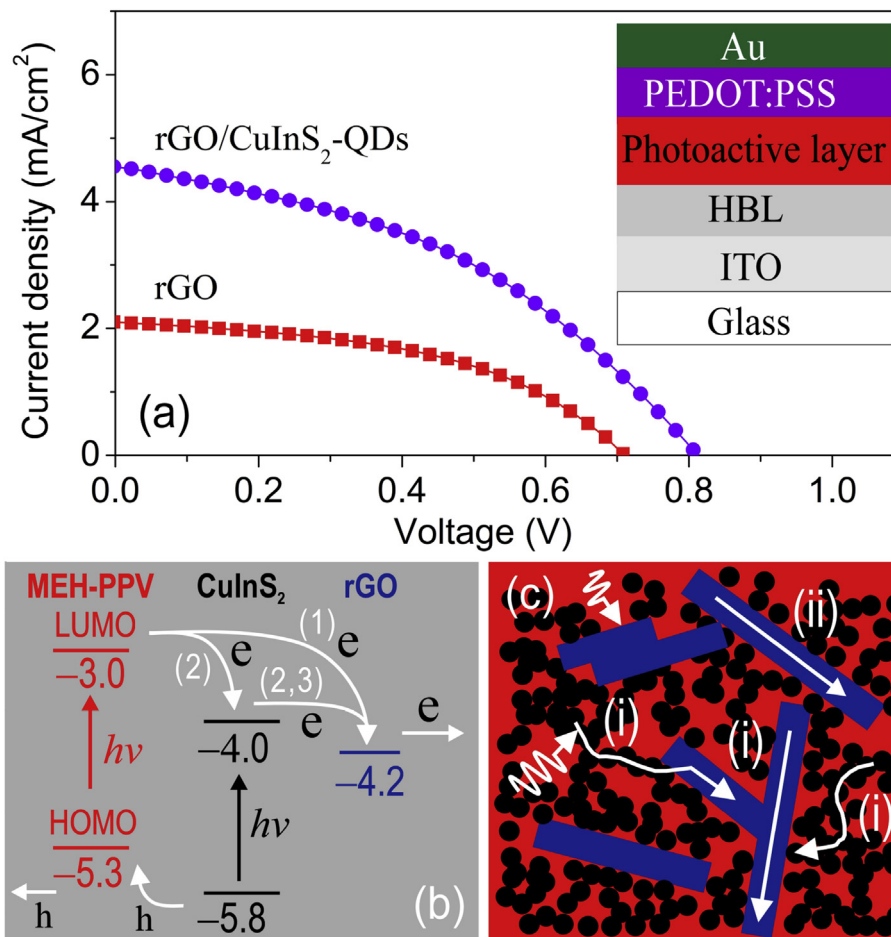

Fig. 7. (a) Typical J–V curves of the solar cells based on rGO and rGO/CuInS$_2$-QDs. (b) Band level (eV) alignments and charge transfer processes in MEH-PPV/rGO-CuInS$_2$ solar cells. (c) Proposed nanomorphology in the solar cells. The inset to (a) shows the solar cell architecture. In plot (c), the blue blocks stand for graphene sheets and the black dots mean the CuInS$_2$-QDs, the zig-zag arrows represent the effective polymer exciton diffusions toward dissociation interfaces, the straight and curved arrows (i) indicate the effective electron transports via continuous nanochannels for photocurrent generation, and the straight arrow (ii) depicts the electron transports on isolated or flat-on configured graphene sheets that are ineffective for photocurrent generation. (A color version of this figure can be viewed online.)

the CuInS$_2$-QDs aggregates on rGO sheets also create additional MEH-PPV/CuInS$_2$ interfaces for the dissociation of the excitons generated by MEH-PPV in the regions far away from MEH-PPV/rGO interface. The presence of additional MEH-PPV/CuInS$_2$ and CuInS$_2$/rGO interfaces makes the rGO/CuInS$_2$-QDs hybrid much more efficient than pure rGO for the dissociation of the excitons

generated in MEH-PPV (Fig. S7). Furthermore, the formation of continuous and highly condensed CuInS$_2$-QDs nanochannels facilitates the transport of the electrons generated at the MEH-PPV/CuInS$_2$ interface into rGO for photocurrent generation. The presence of CuInS$_2$-QDs aggregates on graphene sheets may prevent the graphene sheets from aggregation and reduce the flat-on

Table 2
Solar cell performance measured under AM1.5 illumination (100 mW/cm^2) in ambient conditions.[a]

Sample	V_{oc}(V)	J_{sc}(mA/cm^2)	FF (%)	η (%)	R_s (kΩ)[b]	R_{sh} (kΩ)[b]
rGO	0.69 ± 0.04	2.18 ± 0.15	47.28 ± 4.68	0.71 ± 0.01	1.73 ± 0.71	30.34 ± 6.12
rGO/CuInS$_2$-QDs	0.85 ± 0.04	4.46 ± 0.30	43.26 ± 4.29	1.48 ± 0.03	2.03 ± 0.25	20.23 ± 6.50

[a] Each of the photovoltaic performance data with standard deviations represents the average of three devices that are measured.
[b] R_s and R_{sh} are the series resistance and shunt resistance linked with the slope characteristics at V_{oc} and J_{sc}, respectively.

configuration with graphene sheets lying parallel to the film plane that is unfavorable for photocurrent generation. Therefore, the higher photocurrent generation in the MEH-PPV/rGO-CuInS$_2$ devices than that in the MEH-PPV/rGO cells originates from the combined contributions of the CuInS$_2$-QDs aggregates on rGO sheets, that is, providing complementary absorption, creating additional MEH-PPV/CuInS$_2$ and CuInS$_2$/rGO interfaces for exciton dissociation and charge transfer, forming continuous and highly condensed interpenetrating CuInS$_2$-QDs nanochannels for effective electron transport toward rGO and further to collection electrode, and reducing the deficiencies in the counterpart devices of rGO. Obviously, the rGO/CuInS$_2$-QDs hybrid is an effective hybrid electron acceptor in the PSCs with an extended response in visible spectrum by allowing the efficient charge separation for neutral excited states produced on polymer or on CuInS$_2$-QDs.

The MEH-PPV/rGO-CuInS$_2$ solar cells have a V_{oc} larger than that of the MEH-PPV/rGO devices. It has been demonstrated that the extra electron transfer from CuInS$_2$-QDs to graphene will reduce the W_f of graphene sheet by shifting the Fermi level of conduction band towards the vacuum level [12,60,61], and the adsorption of metal cations can also significantly reduce the W_f of graphene sheets [12,60]. Normally, the V_{oc} in PSCs correlates with the energy difference between the HOMO level of the donor and the conduction band edge of the acceptor [1,2,62–65]. We think that the V_{oc} in the MEH-PPV/rGO-CuInS$_2$ device is determined by the energy level difference between the W_f value of graphene and the polymer HOMO level, similar to the reported polymer/graphene solar cells [15,16]. Accordingly, the higher V_{oc} in rGO/CuInS$_2$-QDs device originates from the altered electronic property (i.e., reduced W_f) of rGO subjected to the deposition of CuInS$_2$-QDs aggregates, in which the energy level difference between the W_f value of graphene and the polymer HOMO level is enlarged.

It should be noted that, in comparison to the MEH-PPV/rGO devices, the formation of CuInS$_2$-QDs aggregates leads to a reduced FF in the MEH-PPV/rGO-CuInS$_2$ cells (Table 2). FF value characterizes the squareness of J–V curves and reflects eventually the transport efficiency of charge carriers to electrodes. Normally, FF is related to the series resistance (R_s) and shunt resistance (R_{sh}) in solar cells, and there are $R_s = 0$ and $R_{sh} = \infty$ in an ideal situation (FF = 1) [66–68]. The R_s is dependent on the resistances of photoactive layer and electrode, along with the contact resistances at each of interfaces, while the R_{sh} correlates with the leakage currents across the cells induced by the pinholes and charge recombination. Our results (Table 2) show that, in comparison to the MEH-PPV/rGO devices, the presence of CuInS$_2$-QDs aggregates produces an almost unchanged R_s but a reduced R_{sh} in the MEH-PPV/rGO-CuInS$_2$ cells. Therefore, the smaller FF in the MEH-PPV/rGO-CuInS$_2$ cells is due to the reduced R_{sh}, for which the original reason is attributed to the creation of additional polymer/CuInS$_2$ interfaces for charge recombination. Since the efficiency of solar cells is determined by the relationship $\eta = J_{sc} \times V_{oc} \times FF/P_{in}$, where P_{in} is incident light power density, the MEH-PPV/rGO-CuInS$_2$ solar cells have a much higher efficiency than MEH-PPV/rGO ones because of the significantly increased J_{sc} and V_{oc} even with a reduced FF. Clearly, rGO/CuInS$_2$-QDs hybrid is a much more efficient electron acceptor than rGO.

4. Conclusion

A rGO/CuInS$_2$-QDs hybrid was synthesized, by a facile one-pot solvothermal approach in which the growth of CuInS$_2$-QDs on GO sheets and the reduction of GO sheets occur simultaneously. It is found that adsorption of partial Cu^{2+} cations in reaction mixture takes place at epoxy/hydroxyl groups on GO sheets, and the adsorbed Cu^{2+} cations provide the nucleation for surface growth of CuInS$_2$-QDs into 3-D aggregates on GO sheets that are reduced into rGO sheets at the same time; moreover, the growth of CuInS$_2$-QDs aggregates facilitates the GO reduction. It is demonstrated that the rGO/CuInS$_2$-QDs hybrid is an effective electron acceptor for PSCs with a complementary absorption property for a broad spectral response extending to 850 nm, much more efficient than rGO, by allowing the efficient charge separation for neutral excited states produced either on polymer or on CuInS$_2$-QDs and reducing the deficiencies in the counterpart devices of rGO. The V_{oc} in the MEH-PPV/rGO-CuInS$_2$ solar cells is mainly determined by the W_f of rGO and the HOMO of polymer MEH-PPV, and the deposition of CuInS$_2$-QDs aggregates increases the energy difference between the W_f value of rGO and the polymer HOMO for a higher V_{oc}; the increased photocurrent generation in the ternary solar cells is attributed to the complementary absorption, the additional polymer/CuInS$_2$ and CuInS$_2$/rGO interfaces for exciton dissociation and the effective interpenetrating CuInS$_2$-QDs nanochannels for charge transports, which are provided by the CuInS$_2$-QDs aggregates on rGO sheets.

Acknowledgment

Appendix A. Supplementary data

Supplementary data related to this article can be found at http://dx.doi.org/10.1016/j.carbon.2015.09.068.

References

[1] S. Günes, H. Neugebauer, N.S. Sariciftci, Conjugated polymer-based organic solar cells, Chem. Rev. 107 (2007) 1324–1338.
[2] H.L. Yip, A.K.Y. Jen, Recent advances in solution-processed interfacial materials for efficient and stable polymer solar cells, Energy Environ. Sci. 5 (2012) 5994–6011.
[3] M.D. Stoller, S.J. Park, Y. Zhu, J. An, R.S. Ruoff, Graphene-based ultracapacitors, Nano Lett. 8 (2008) 3498–3502.
[4] K.I. Bolotin, K.J. Sikes, Z. Jiang, M. Klima, G. Fudenberg, J. Hone, et al., Ultrahigh electron mobility in suspended graphene, Solid State Commun. 146 (2008) 351–355.
[5] C. Lee, X. Wei, J.W. Kysar, J. Hone, Measurement of the elastic properties and intrinsic strength of monolayer graphene, Science 321 (2008) 385–388.
[6] A.A. Balandin, S. Ghosh, W. Bao, I. Calizo, D. Teweldebrhan, F. Miao, et al., Superior thermal conductivity of single-layer graphene, Nano Lett. 8 (2008) 902–907.

[7] R.R. Nair, P. Blake, A.N. Grigorenko, K.S. Novoselov, T.J. Booth, T. Stauber, et al., Fine structure constant defines visual transparency of graphene, Science 320 (2008) 1308.

[8] K.S. Novoselov, V.I. Fal'ko, L. Colombo, P.R. Gellert, M.G. Schwab, K. Kim, A roadmap for graphene, Nature 490 (2012) 192–200.

[9] X. Huang, Z. Zeng, Z. Fan, J. Liu, H. Zhang, Graphene-based electrodes, Adv. Mater. 24 (2012) 5979–6004.

[10] M. He, J. Jung, F. Qiu, Z. Lin, Graphene-based transparent flexible electrodes for polymer solar cells, J. Mater. Chem. 22 (2012) 24254–24264.

[11] S.S. Li, K.H. Tu, C.C. Lin, C.W. Chen, M. Chhowalla, Solution-processable graphene oxide as an efficient hole transport layer in polymer solar cells, ACS Nano 4 (2010) 3169–3174.

[12] J. Liu, Y. Xue, Y. Gao, D. Yu, M. Durstock, L. Dai, Hole and electron extraction layers based on graphene oxide derivatives for high-performance bulk heterojunction solar cells, Adv. Mater. 24 (2012) 2228–2233.

[13] S. Qu, M. Li, L. Xie, X. Huang, J. Yang, N. Wang, et al., Noncovalent functionalization of graphene attaching [6,6]-phenyl-C61-butyric acid methyl ester (PCBM) and application as electron extraction layer of polymer solar cells, ACS Nano 7 (2013) 4070–4081.

[14] J. Liu, Y. Xue, L. Dai, Sulfated graphene oxide as a hole-extraction layer in high-performance polymer solar cells, J. Phys. Chem. Lett. 3 (2012) 1928–1933.

[15] Z. Liu, Q. Liu, Y. Huang, Y. Ma, S. Yin, X. Zhang, et al., Organic photovoltaic devices based on a novel acceptor material: graphene, Adv. Mater. 20 (2008) 3924–3930.

[16] Q. Liu, Z. Liu, X. Zhang, L. Yang, N. Zhang, G. Pan, et al., Polymer photovoltaic cells based on solution-processable graphene and P3HT, Adv. Funct. Mater. 19 (2009) 894–904.

[17] P.T. Yin, S. Shah, M. Chhowalla, K.B. Lee, Design, synthesis, and characterization of graphene-nanoparticle hybrid materials for bioapplications, Chem. Rev. 115 (2015) 2483–2531.

[18] W.I. Park, C.H. Lee, J.M. Lee, N.J. Kim, G.C. Yi, Inorganic nanostructures grown on graphene layers, Nanoscale 3 (2011) 3522–3533.

[19] H. Bai, C. Li, G. Shi, Functional composite materials based on chemically converted graphene, Adv. Mater. 23 (2011) 1089–1115.

[20] N. Li, M. Cao, C. Hu, Review on the latest design of graphene-based inorganic materials, Nanoscale 4 (2012) 6205–6218.

[21] X. An, J.C. Yu, Graphene-based photocatalytic composites, RSC Adv. 1 (2011) 1426–1434.

[22] X. Huang, Z. Yin, S. Wu, X. Qi, Q. He, Q. Zhang, et al., Graphene-based materials: synthesis, characterization, properties, and applications, Small 7 (2011) 1876–1902.

[23] X. Geng, L. Niu, Z. Xing, R. Song, G. Liu, M. Sun, et al., Aqueous-processable noncovalent chemically converted graphene-quantum dot composites for flexible and transparent optoelectronic films, Adv. Mater. 22 (2010) 638–642.

[24] H.J. Lewerenz, Development of copperindiumdisulfide into a solar material, Sol. Energy Mater. Sol. Cells 83 (2004) 395–407.

[25] R. Klenk, J. Klaer, R. Scheer, M.C. Lux-Steiner, I. Luck, N. Meyer, et al., Solar Cells Based on CuInS₂ – an overview, Thin Solid Films 480–481 (2005) 509–514.

[26] S. Han, M. Kong, Y. Guo, M. Wang, Synthesis of copper indium sulfide nanoparticles by solvothermal method, Mater. Lett. 63 (2009) 1192–1194.

[27] W. Yue, F. Wu, C. Liu, Z. Qiu, Q. Cui, H. Zhang, et al., Incorporating CuInS₂ quantum dots into polymer/oxide-nanoarray system for efficient hybrid solar cells, Sol. Energy Mater. Sol. Cells 114 (2013) 43–53.

[28] W. Yue, S. Han, R. Peng, W. Shen, H. Geng, F. Wu, et al., CuInS₂ quantum dots synthesized by a solvothermal route and their application as effective electron acceptors for hybrid solar cells, J. Mater. Chem. 20 (2010) 7570–7578.

[29] E. Arici, N.S. Sariciftci, D. Meissner, Hybrid solar cells based on nanoparticles of CuInS₂ in organic matrices, Adv. Funct. Mater. 13 (2003) 165–171.

[30] A. Lefrançois, B. Luszczynska, B. Pepin-Donat, C. Lombard, B. Bouthinon, J.M. Verilhac, et al., Enhanced charge separation in ternary P3HT/PCBM/CuInS₂ nanocrystals hybrid solar cells, Sci. Rep. 5 (2015) 7768.

[31] T. Rath, M. Edler, W. Haas, A. Fischereder, S. Moscher, A. Schenk, et al., A direct route towards polymer/copper indium sulfide nanocomposite solar cells, Adv. Energy Mater. 1 (2011) 1046–1050.

[32] E. Maier, T. Rath, W. Haas, O. Werzer, R. Saf, F. Hofer, et al., CuInS₂–poly(3-(ethyl-4-butanoate)thiophene) nanocomposite solar cells: preparation by an in situ formation route, performance and stability issues, Sol. Energy Mater. Sol. Cells 95 (2011) 1354–1361.

[33] C. Fradler, T. Rath, S. Dunst, I. Letofsky-Papst, R. Saf, B. Kunert, et al., Flexible polymer/copper indium sulfide hybrid solar cells and modules based on the metal xanthate route and low temperature annealing, Sol. Energy Mater. Sol. Cells 124 (2014) 117–125.

[34] L. Zhou, X. Yang, B. Yang, X. Zuo, G. Li, A. Feng, et al., Controlled synthesis of CuInS₂/reduced graphene oxide nanocomposites for efficient dye-sensitized solar cells, J. Power Sources 272 (2014) 639–646.

[35] S. Wang, Y. Zhu, X. Yang, C. Li, Photoelectrochemical detection of H₂O₂ based on flower-like CuInS₂–graphene hybrid, Electroanalysis 26 (2014) 573–580.

[36] W.S. Hummers, R.E. Offeman, Preparation of graphitic oxide, J. Am. Chem. Soc. 80 (1958) 1339.

[37] C. Chen, M. Wang, K. Wang, Characterization of polymer/TiO₂ photovoltaic cells by intensity modulated photocurrent spectroscopy, J. Phys. Chem. C 113 (2009) 1624–1631.

[38] X. Zhang, F. Xu, B. Zhao, X. Ji, Y. Yao, D. Wu, et al., Synthesis of CdS quantum dots decorated graphene nanosheets and non-enzymatic photoelectrochemical detection of glucose, Electrochim. Acta 133 (2014) 615–622.

[39] B. Zhao, J. Song, P. Liu, W. Xu, T. Fang, Z. Jiao, et al., Monolayer graphene/NiO nanosheets with two-dimension structure for supercapacitors, J. Mater. Chem. 21 (2011) 18792–18798.

[40] J. Zhang, Z. Xiong, X.S. Zhao, Graphene–metal–oxide composites for the degradation of dyes under visible light irradiation, J. Mater. Chem. 21 (2011) 3634–3640.

[41] C. Fu, G. Zhao, H. Zhang, S. Li, Evaluation and characterization of reduced graphene oxide nanosheets as anode materials for lithium-ion batteries, Int. J. Electrochem. Sci. 8 (2013) 6269–6280.

[42] C. Nethravathi, T. Nisha, N. Ravishankar, C. Shivakumara, M. Rajamathi, Graphene–nanocrystalline metal sulphide composites produced by a one-pot reaction starting from graphite oxide, Carbon 47 (2009) 2054–2059.

[43] C. Xu, X. Wang, J. Zhu, Graphene–metal particle nanocomposites, J. Phys. Chem. C 112 (2008) 19841–19845.

[44] D. Luo, G. Zhang, J. Liu, X. Sun, Evaluation criteria for reduced graphene oxide, J. Phys. Chem. C 115 (2011) 11327–11335.

[45] F.M. Courtel, A. Hammami, R. Imbeault, G. Hersant, R.W. Paynter, B. Marsan, et al., Synthesis of n-type CuInS₂ particles using N-methylimidazole, characterization and growth mechanism, Chem. Mater. 22 (2010) 3752–3761.

[46] S. Peng, J. Liang, L. Zhang, Y. Shi, J. Chen, Shape-controlled synthesis and optical characterization of chalcopyrite CuInS₂ microstructures, J. Cryst. Growth 305 (2007) 99–103.

[47] Y. Wang, N. Herron, Nanometer-sized semiconductor clusters: materials synthesis, quantum size effects, and photophysical properties, J. Phys. Chem. 95 (1991) 525–532.

[48] D.R. Dreyer, S. Park, C.W. Bielawski, R.S. Ruoff, The chemistry of graphene oxide, Chem. Soc. Rev. 39 (2010) 228–240.

[49] K. Yuan, L. Chen, L. Tan, Y. Chen, Performance enhancement of bulk heterojunction solar cells with direct growth of CdS-cluster-decorated graphene nanosheets, Chem. Eur. J. 20 (2014) 1–10.

[50] S. Sun, W. Wang, L. Zhang, Bi₂WO₆ quantum dots decorated reduced graphene oxide: improved charge separation and enhanced photoconversion efficiency, J. Phys. Chem. C 117 (2013) 9113–9120.

[51] G. Sobon, J. Sotor, J. Jagiello, R. Kozinski, M. Zdrojek, M. Holdynski, et al., Graphene oxide vs. reduced graphene oxide as saturable absorbers for Er-doped passively mode-locked fiber laser, Opt. Express 20 (2012) 19463–19473.

[52] A. Cao, Z. Liu, S. Chu, M. Wu, Z. Ye, Z. Cai, et al., A facile one-step method to produce graphene–CdS quantum dot nanocomposites as promising optoelectronic materials, Adv. Mater. 22 (2010) 103–106.

[53] L.D. Partain, R.A. Schneider, L.F. Donaghey, P.S. Mcleod, Surface chemistry of CuₓS and CuₓS/CdS determined from X-ray photoelectron spectroscopy, J. Appl. Phys. 57 (1985) 5056–5065.

[54] P. Bombicz, I. Mutikainen, M. Krunks, T. Leskelä, J. Madarász, L. Niinistö, Synthesis, vibrational spectra and X-ray structures of copper (I) thiourea complexes, Inorg. Chim. Acta 357 (2004) 513–525.

[55] S. Sarkar, S. Dutta, S. Chakrabarti, P. Bairi, T. Pal, Redox-switchable copper (I) metallogel: a metal-organic material for selective and naked-eye sensing of picric acid, ACS Appl. Mater. Interfaces 6 (2014) 6308–6316.

[56] M. Krunks, T. Leskelä, R. Mannonen, L. Niinistö, Thermal decomposition of copper (I) thiocarbamide chloride hemihydrate, J. Therm. Anal. 53 (1998) 355–364.

[57] A. Kumari, I. Singh, N. Prasad, S.K. Dixit, P.K. Rao, P.K. Bhatnagar, et al., Improving the efficiency of a poly(3-hexylthiophene)-CuInS₂ photovoltaic device by incorporating graphene nanopowder, J. Nanophot. 8 (2014) 083092.

[58] A.J. Breeze, Z. Schlesinger, S.A. Carter, P.J. Brock, Charge transport in TiO₂/MEH-PPV polymer photovoltaics, Phys. Rev. B 64 (2001) 125205.

[59] A. Benayad, H.J. Shin, H.K. Park, S.M. Yoon, K.K. Kim, M.H. Jin, et al., Controlling work function of reduced graphite oxide with Au-ion concentration, Chem. Phys. Lett. 475 (2009) 91–95.

[60] Y. Shi, K.K. Kim, A. Reina, M. Hofmann, L.J. Li, J. Kong, Work function engineering of graphene electrode via chemical doping, ACS Nano 4 (2010) 2689–2694.

[61] J. Zhao, J. Han, J.P. Lu, Work Functions of Pristine and alkali-metal intercalated carbon nanotubes and bundles, Phys. Rev. B 65 (2002) 193401.

[62] K.M. Coakley, M.D. McGehee, Conjugated polymer photovoltaic cells, Chem. Mater. 16 (2004) 4533–4542.

[63] Y. Zhou, M. Eck, M. Krüger, Bulk-heterojunction hybrid solar cells based on colloidal nanocrystals and conjugated polymers, Energy Environ. Sci. 3 (2010) 1851–1864.

[64] T. Xu, Q. Qiao, Conjugated polymer–inorganic semiconductor hybrid solar cells, Energy Environ. Sci. 4 (2011) 2700–2720.

[65] A.J. Moulé, L. Chang, C. Thambidurai, R. Vidu, P. Stroeve, Hybrid solar cells: basic principles and the role of ligands, J. Mater. Chem. 22 (2012) 2351–2368.

[66] A. Moliton, J.M. Nunzi, How to model the behaviour of organic photovoltaic cells, Polym. Int. 55 (2006) 583–600.

[67] W.J. Potscavage Jr., A. Sharma, B. Kippelen, Critical interfaces in organic solar cells and their influence on the open-circuit voltage, Acc. Chem. Res. 42 (2009) 1758–1767.

[68] B. Qi, J. Wang, Fill factor in organic solar cells, Phys. Chem. Chem. Phys. 15 (2013) 8972–8982.